sciendo

Geologos 29, 1 (2023): 1–20
https://doi.org/10.14746/logos.2023.29.1.01

GEOLOGOS

Utilization of ASTER data in lithological and lineament mapping of the southern flank of the Central High Atlas in Morocco

Maryam Errami*, Ahmed Algouti, Abdellah Algouti, Abdelouhed Farah, Saloua Agli

Department of Geology, Geosciences Geotourism Natural Hazards and Remote Sensing Laboratory (2GRNT), University of Cadi Ayyad, Faculty of Sciences Semlalia, BP 2390, 40000, Marrakesh, Morocco
*corresponding author; e-mail: maryam.errami@ced.uca.ma

Abstract

Geological mapping undoubtedly plays an important role in several studies and remote sensing data are of great significance in geological mapping, particularly in poorly mapped areas situated in inaccessible regions. In the present study, Principal Component Analysis (PCA), Band Rationing (BR) and Minimum Noise Fraction (MNF) algorithms are applied to map lithological units and extract lineaments in the Amezri-Amassine area, by using multispectral ASTER image and global digital elevation model (GDEM) data for the first time. Following preprocessing of ASTER images, advanced image algorithms such as PCA, BR and MNF analyses are applied to the 9ASTER bands. Validation of the resultant maps has relied on matching lithological boundaries and faults in the study area and on the basis of pre-existing geological maps. In addition to the PCA image, a new band-ratio image, 4/6–5/8–4/5, as adopted in the present work, provides high accuracy in discriminating lithological units. The MNF transformation reveals improvement over previous enhancement techniques, in detailing most rock units in the area. Hence, results derived from the enhancement techniques show a good correlation with the existing litho-structural map of the study area. In addition, the present results have allowed to update this map by identifying new lithological units and structural lineaments. Consequently, the methodology followed here has provided satisfactory results and has demonstrated the high potential of multispectral ASTER data for improving lithological discrimination and lineament extraction.

Key words: Amezri-Amassine area, PCA, band ratio, MNF, automatic lineament extraction

1. Introduction

During the last decade, numerous studies have demonstrated the applicability of ASTER data for geological mapping (see e.g., Othman & Gloaguen, 2017; Bentahar & Raji, 2021; Farah et al., 2021), thanks to the high number of bands in the Short Wave Infrared (SWIR) region (six spectral bands for ASTER sensor in comparison to only one SWIR band of Landsat sensor; see Hewson et al., 2017; Othman & Gloaguen, 2017). In addition to its high spatial resolution, the ASTER sensor provides a unique combination of covering multiple spectral regions (visible to Near-Infrared VNIR, SWIR and Thermal Infrared TIR regions) (Amer et al., 2016), which increases the ability of ASTER data to discriminate rock units and minerals on the Earth's surface spectrally. Several authors have mentioned the complementarity of VNIR, SWIR and TIR wavelength regions in lithological mapping. For example, the VNIR wavelength region distinguish transition metals such as iron oxides (goethite, hematite, jarosite) and Rare Earth Elements (REEs) (Rowan et al., 1986), while the SWIR wavelength region yields some information on the presence of strata bearing minerals (phyllosilicates, clays) and carbonates

(Hunt, 1977). Furthermore, the TIR wavelength region allows discrimination between carbonates and silicate minerals (Salisbury & Walter, 1989). Based on these characteristics, the ASTER data have been widely and increasingly used in geological and mineralogical research (Shirmard et al., 2020; Imran et al., 2022).

Several digital processing techniques are used to extract useful information from ASTER images. Çörtük et al. (2020) proved that PCA, BR and MNF were extremely powerful techniques, successfully used in mapping ophiolitic rocks in central Anatolia (Turkey). In addition, Ge et al. (2018) adopted PC4, PC3 and PC1 for preparation of a colour combination, which proved helpful in mapping the ophiolite complex in Inner Mongolia (China).

The BR method is widely used for geological mapping and has proved its usefulness for lithological discrimination, due to its capability to highlight spectral features and to reduce the albedo effects. For example, Morsli et al. (2021) mapped the lithology of pegmatitic rocks in the Zenaga area (Morocco), by using novel band ratio combinations (1/4; 6/3; 2/5) of ASTER data. In addition, mafic and ultramafic rocks in central Anatolia (Turkey) were mapped by Çörtük et al. (2020), who used 4/8, 2/1 and 3/4 band ratios of ASTER data.

The Amezri-Amassine area in Morocco is one of the best places to study Mesozoic rocks. However, some geological features are situated in inaccessible areas, which explains the need for remote sensing data in their detection, which have so far been rarely used in the geological mapping of the area. The purpose of the present study is to show that a combination of methods used can be successfully applied here as an alternative to traditional field work. It aims to evaluate the performance of ASTER data in the mapping of lineaments and lithologies, using some methods that have been already employed by many authors in other regions. The approach adopted will permit the identification of new rock units and structural lineaments in the Amezri-Amassine area, which in their turn provide additional data to the regional and general geology of Morocco. We also highlight the role of digital processing, especially PCA, spectral BR and MNF, to enhance the lithological discrimination of rock units in the study area. In addition, we have compared the results of these techniques for processing the ASTER images used in the present work. The contribution of directional edge-detection filtering and shading relief for obtaining a more reliable analysis and interpretation of lineaments is recognised herein.

2. Geological setting

The Amezri-Amassine area is situated in the southwestern corner of the Central High Atlas (CHA) belt, immediately adjacent to the transition with the Marrakech High Atlas Belt (Fig. 1A, B). Covering an area of approximately 2,218 km^2, it is located between latitudes 350,320 and 346,317, and between longitudes 740,546 and 780,037 (Fig. 1C). It is characterised by peaks varying in elevation between 1,434 m and 4,049 m a.s.l., with the Amassine and Ighiln'Oumgoun mountains as summits.

The CHA belt formed phasewise during three orogenic cycles. It has a thick Mesozoic cover, consisting mainly of Lower and Middle Jurassic deposits (Fig. 2) (de Jong et al., 2008). This sequence was initiated by deposition of Triassic siliciclastic strata with basaltic formations, which crop out mainly along major faults. The Lower Jurassic is characterised by a several metre-thick carbonate sequence, deposited in shallow-marine settings, overlain by a succession of limestones, calciturbidites and shales, dated as Middle Jurassic (Fig. 3) (Ait Addi & Chafiki, 2013). These formations are covered by Upper Jurassic terrestrial formations with magmatic intrusions (de Jong et al., 2008). The Cretaceous succession starts with red sandstones and conglomerates of Cenomanian age, followed by platform limestones of Cenomanian-Turonian date (Ettachfini et al., 2005). These marine deposits are overlain by a terrestrial to lacustrine succession, dated as Late Cretaceous to Paleogene, which are covered by Miocene-Pliocene terrestrial strata (Marzoqi & Pascal, 2000). The crystalline basement comprises Precambrian and Palaeozoic meta-sedimentary rocks (Fig. 3), affected by an ENE-trending normal faulting. Partly inherited from the Panafrican or Variscan orogeny, this structural pattern controlled the Jurassic sedimentation by vertical and strike-slip faulting (de Jong et al., 2008).

From north to south, the Amezri-Amassine area includes the axial part of the CHA and the southern Sub-Atlasic zone. The northern part is dominated by Triassic and Jurassic rocks, which are characterised mainly by sedimentary rocks with minor intercalations of basaltic rocks (Fig. 2). Capped by basaltic and dolerite formation, the Triassic deposits are made up mostly of siltstones, fine-grained sandstones and, locally, evaporites. Dolerite lavas effusing within the red-beds that filled sedimentary basins were associated with Triassic fracturing (Jacobshagen et al., 1988). These siliciclastic sediments are overlain by Lower Jurassic carbonates and evaporites, which are in turn followed by Middle and Upper Jurassic clastic terrestrial deposits

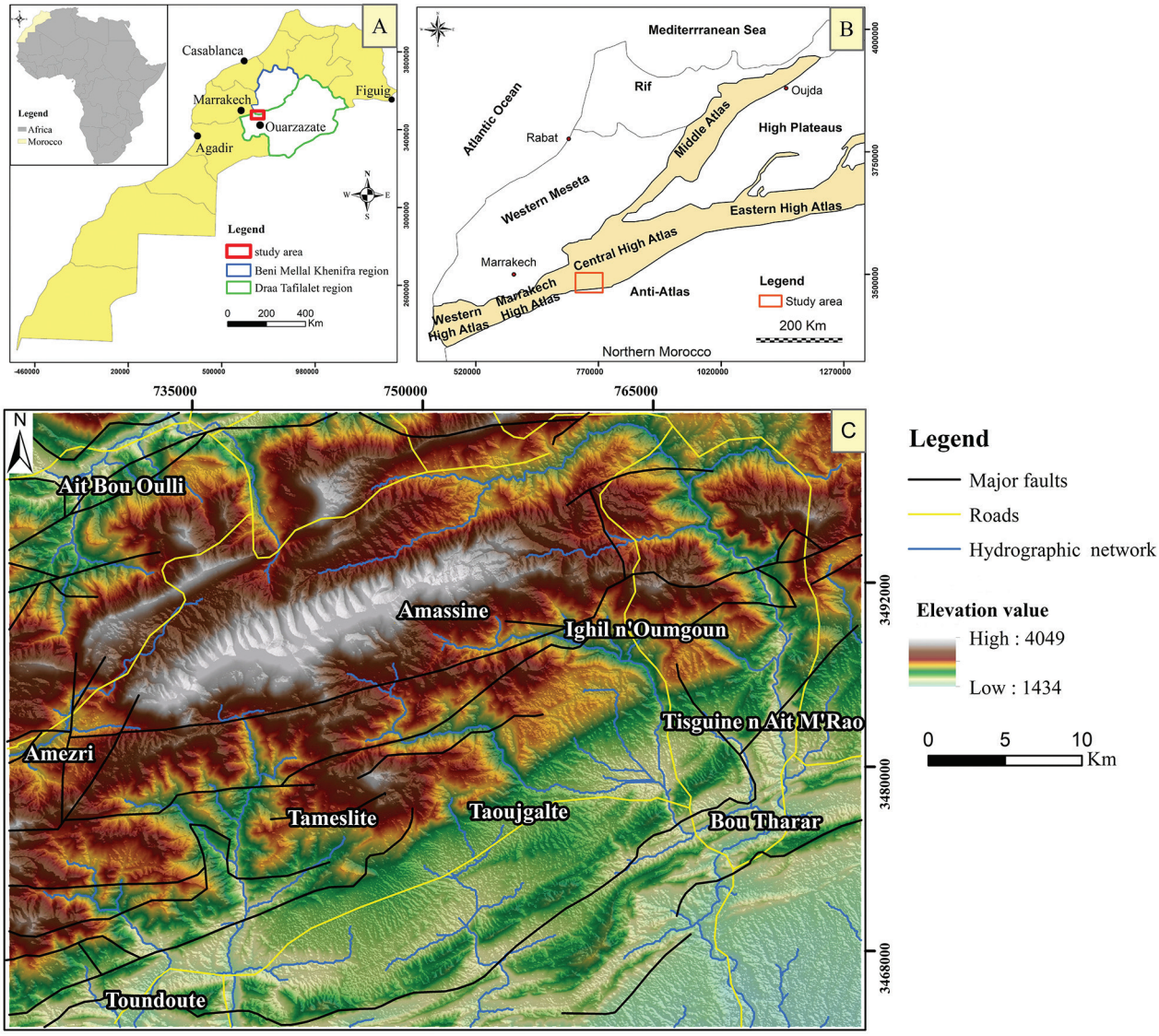

Fig. 1. Location of the study area. **A –** National view; **B –** Regional view; **C –** 3D elevation map of the Amezri-Amassine area.

(Fig. 3). Trachyandesitic lava flows, resulting from the early manifestation of Middle Jurassic magma, are intercalated within the Middle Jurassic deposits in this area (Skikraet al., 2021). The Mesozoic cover of the axial part is bordered to the west by Cambro-Ordovician shales and pelites, as well as by black shales of Precambrian age (Fig. 2).

The Mesozoic formations of this part are affected by a W-E to WSW-ENE directional trend which corresponds to multi-kilometre-long faults (Fig. 2), with normal activity during the Triassic and Early Jurassic (Piqué et al., 1998) or with reverse during Cenozoic times. However, the northeast trending faults are also interpreted to have acted as transcurrent faults during this period by other authors (Laville & Piqué, 1992). In addition to thrusting, W-E to ENE fold axes have been described from this region and attributed to the compressive phase (Piqué et al., 1998). The folding has also played an important role during Cenozoic compression, having been strongly controlled by lithological factors (Missenard et al., 2007).

The southern sub-Atlasic zone is subdivided from north to south into two parts: the northern part corresponding to the Toundoutenappe, and the southern part, corresponding to the folds and large slabs of the phosphate succession (Benammi & Toto, 2005). The latter includes terrestrial and marine strata, ranging in age from Late Cretaceous to Late Eocene (Fig. 3) and folded and cut into large slabs by a family of subequatorial to NE-SW-trending faults (Benammi et al., 2001). These stacked lay-

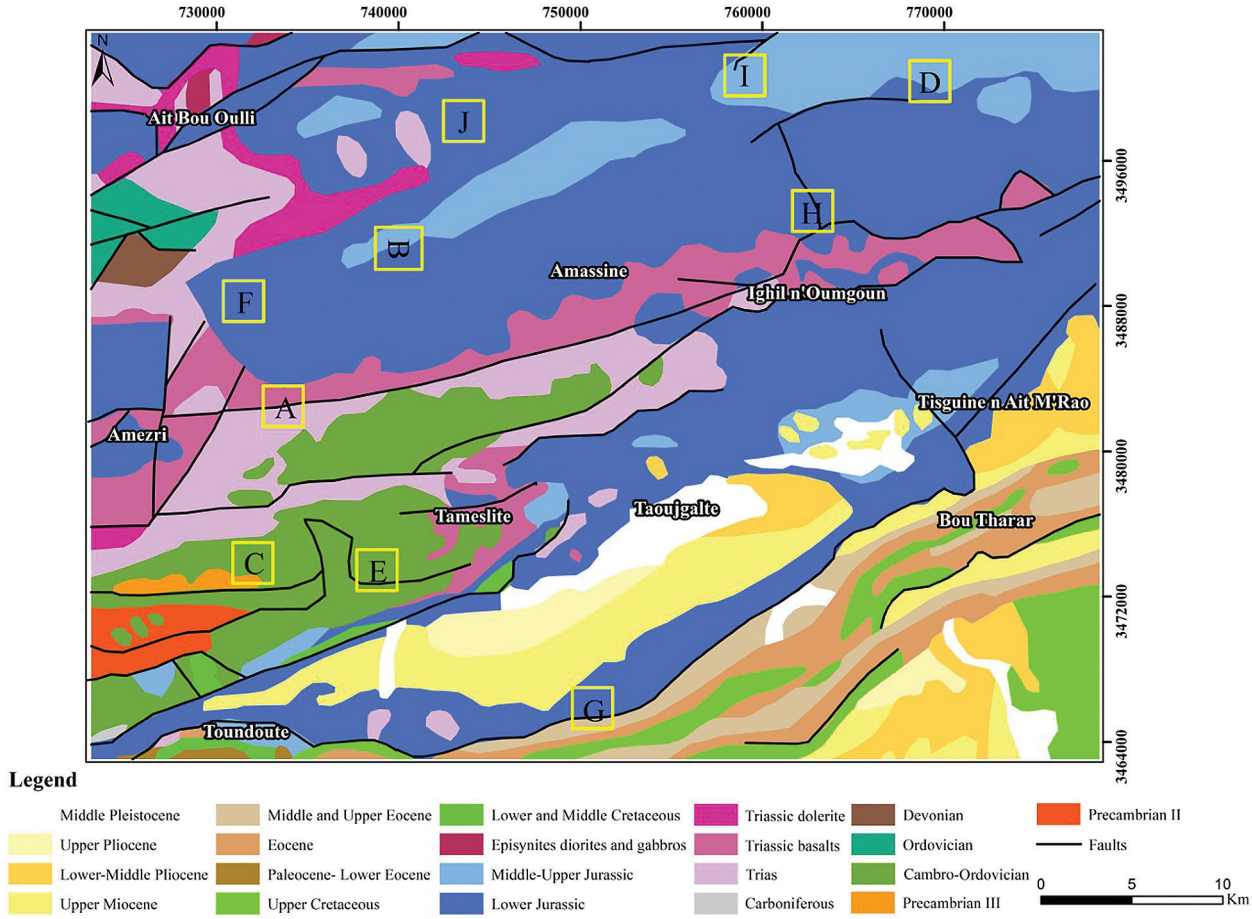

Fig. 2. The geological sketch of Amezri-Amassine area based on the geological map of Morocco 1:1,000,000.

ers slid down from the southern sub-Atlasic zone onto the recent deposits of the Ouarzazate basin, whereas the Jurassic carbonate pile of Toundoutenappe was sheared off from the Triassic deposits and overthrust, towards the south, the marginal zone phosphate succession (Jacobshagen et al., 1988). This decollement of the cover is a consequence of Cenozoic crustal shortening which is also marked in this region by several steeply dipping reverse faults that affect both basement rocks and cover (Laville & Piqué, 1992). In addition, this part is characterised by folds and continuous huge thrusts, referred to by many authors as the 'South Atlasic Fault'(near Toundoute) (Fig. 2) (Elleroet al., 2020).

Following digitization of the main lithostratigraphical units and of the major faults of the geological map of Morocco, at 1:1,000.000 scales, two maps covering the study area have been produced (Figs. 2, 4A). A statistical study has revealed the presence of 37 structural lineaments (faults and thrusts), ranging in length between 1.9 and 54.95 km (Fig. 4A–C). Their rose diagram shows two dominant directions: W-E and WSW-ENE (Fig. 4D). The fault data and lithological map were used in the present work as a reference for defining lithological and local structural features. Furthermore, to improve our results, these two maps (Figs. 2, 4) are used to check and validate both the lineaments and lithological maps.

3. Material and methods

The present study uses remote sensing data, particularly multispectral bands and GDEM data of ASTER satellite, to map lithological units and lineament structures. The Advanced Spaceborne Thermal Emission and Reflection Radiometer (ASTER) is a high spectral, radiometric and spatial resolution multispectral sensor (Amer et al., 2016). It presents a wide spectral coverage, by collecting and recording emitted and reflected Electromagnetic Radiation (RMR) in 14 spectral bands (Table 1). The visible and near-infrared (VNIR) region has three recording channels at wavelengths between 0.52 and 0.86 µm, with a spatial resolution of 15 m, six bands in the short-wave infrared (SWIR) portion of the electromagnetic spectrum, with a 30-m spatial

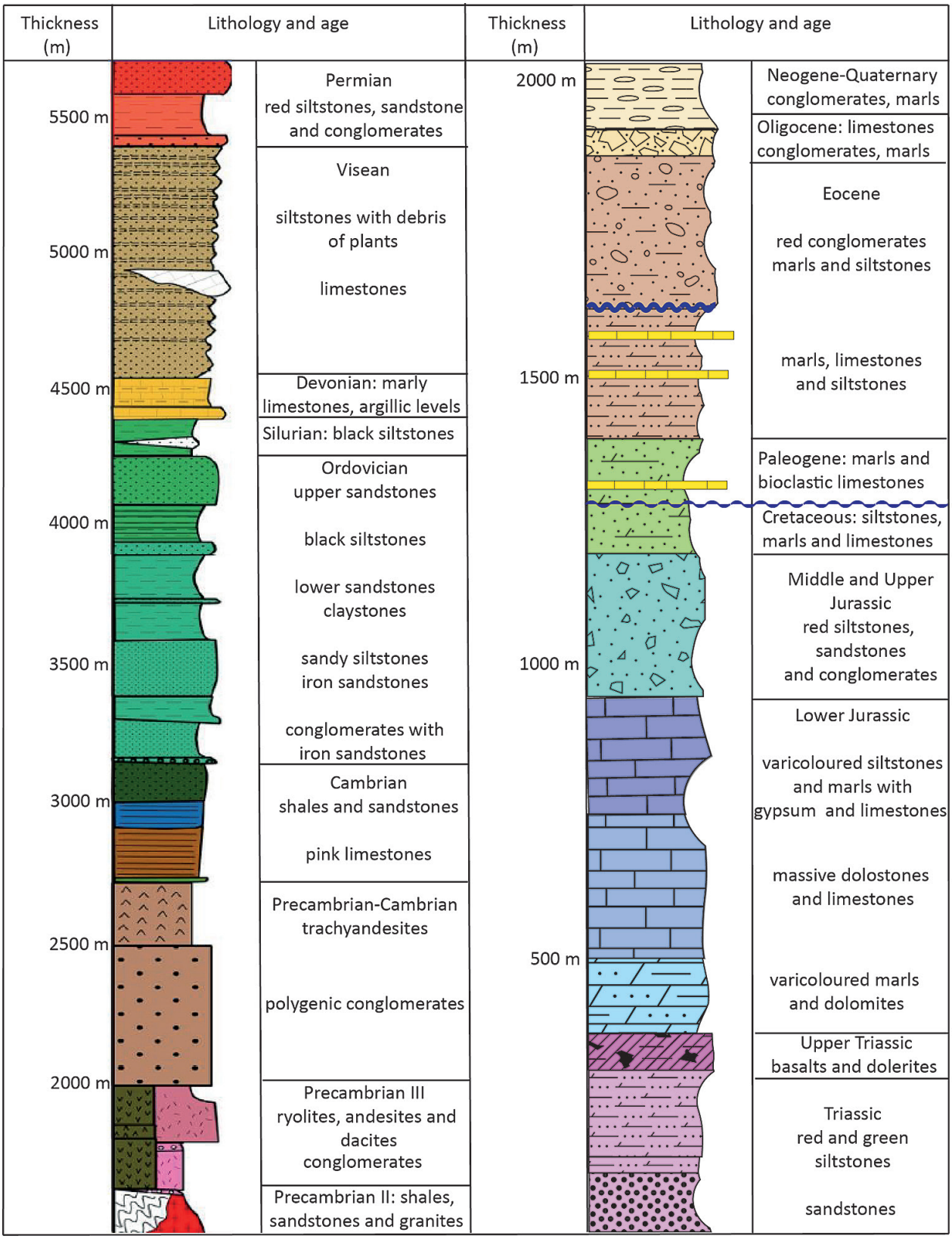

Fig. 3. Generalised stratigraphy of the CHA rocks (Michard et al., 2008).

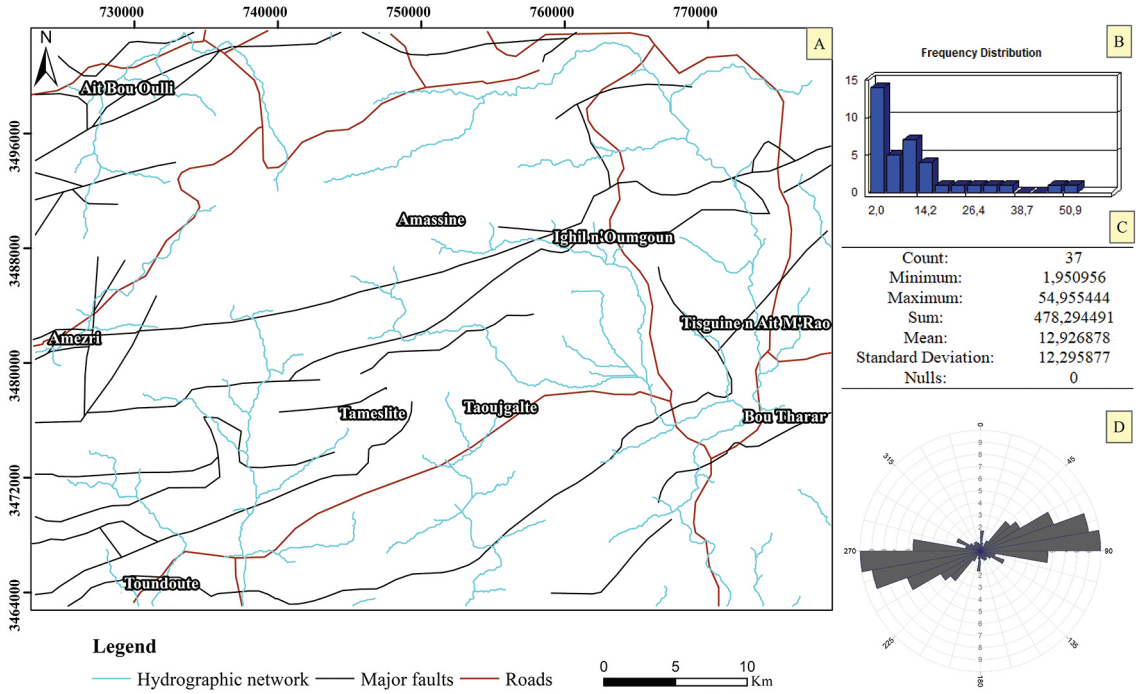

Fig. 4. A –Faults digitized from the geological map of the study area; **B –**Length frequency diagram of lineaments; **C –** Basic statistics of faults digitized; **D –** Rose diagram of faults.

resolution. ASTER sensor measures also emitted radiation (thermal infrared) in five bands between 8.125 and 11.65 µm, with a 90-m spatial resolution (Table 1). ASTER data yield the possibility of applying many image-processing algorithms, with scenes of 60 x 60 km in the swath width.

The ASTER image used in the present work was obtained on September 20, 2020 at the L1B (radiance to sensor) level, with a projection Universal Transverse Mercator (UTM) zone 29 North and a World Geodetic System WGS 84 datum. This image was acquired from US Geological EROS (http://glovis.usgs.gov/), with excellent weather conditions and 0% cloud cover.

The methodology used here also integrates ASTER GDEM, which yields geomorphological and structural information, for lineament extraction. ASTER GDEM is frequently used to identify structural features automatically, thanks to its high radiometric sensitivity (Khodadadi & Arfania, 2017; Bentahar & Raji, 2021). In the present study, the ASTERGDEM image, covering the target area, has been used to generate the average elevation of the terrain. Figure 1C displays a hypsometric map with pseudocolours related to elevations in the study area.

We here apply remote sensing techniques to ASTER satellite data in order to map geological units and extract lineaments automatically. The whole experiment was divided into two steps, including lithological mapping and lineament extraction. Several techniques are used to extract lineaments namely automatic, semi-automatic and manual extractions (Adiri et al., 2017). Lithological mapping and extraction of lineaments requires some rigorous pre-processing of the ASTER satellite image, that reduces the effects of geometric distortions as well as multiplicative and additive atmospheric effects, during data acquisition.

Table 1. Spectral characteristics of ASTER bands used in the present study.

Subsystem of ASTER	VNIR	SWIR
Spectral range	1 0.52–0.60 (0.56) 2 0.63–0.69 (0.66) 3 N 0.78–0.86 (0.82) 3 B 0.78–0.86 (0.82)	4 1.60–1.70 (1.650) 5 2.145–2.185 (2.165) 6 2.185–2.225 (2.205) 7 2.235–2.285 (2.260) 8 2.295–2.365 (2.330) 9 2.360–2.430 (2.395)
Spatial resolution	15 m	30 m

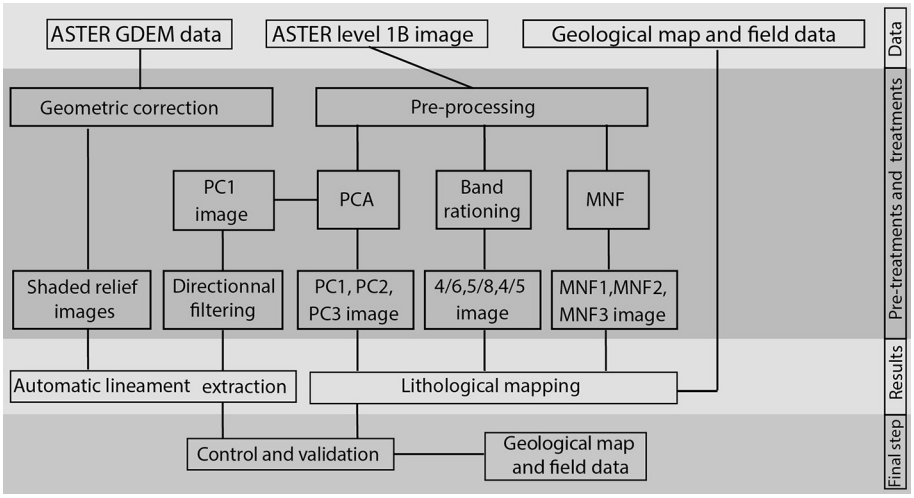

Fig. 5. Flow chart of the methodology used in the present paper.

This preliminary processing step involved radiometric calibration and atmospheric correction, which was achieved by using the Fast Line of Sight Atmospheric Analysis Spectral Hypercubes (FLAASH) model, embedded in ENVI 5.2 software. These corrections provide images corrected for additive atmospheric effects. In addition, the GDEM data were subjected to geometric correction in order to remove geometric distortion by using ground control points. Selecting some points located on the ASTER GDEM and reprojecting them to appropriate co-ordinate system, of the current orthographic database (Google), allows to eliminate the effects of geometric distortion, which are related to the speed and height of the sensor on the orbit (Zhao et al., 2021).

After the necessary corrections, the ASTER image has been further subjected to various digital processing, especially, PCA, BR and MNF transformation, in order to reduce noise and improve the ability of lithological discrimination. Secondly, a first principal component was derived from the nine ASTER bands. From the PC1, previously obtained, four directional images were generated by using Envi software. ASTER GDEM data have further been subjected to shading relief, by applying the hill-shading tool of ArcGIS 10.2. After that, the four filtered images and shaded relief images underwent the automatic extraction process, with the help of the line-model tool of Geomatica Software. This tool has been widely used for automatic lineament extraction (Muavhi & Mavhungu, 2020; Farah et al., 2021).

Subsequently, statistical analysis was achieved by determining numbers, lengths and trends of extracted lineaments. The rose diagram, which is frequently used for lineament analysis, served to determine the pattern of linear structures, based on their direction. It was performed by means of the Rockworks 17 software. Figure 5 illustrates the data and methodology adopted here.

4. Digital image processing

4.1. Principal Component Analysis

PCA is a multivariate statistical technique that can be applied to remove the redundancy and irradiance effects of satellite data (Ge et al., 2018; Sheikhrahimi et al., 2019; Çörtük et al., 2020; Beygi et al., 2021; Traore et al., 2022). PCA was used in the present study to select the best principal components of ASTER images, for mapping lithological units and lineaments in the Amezri-Amassine area. PCA is widely used for lithological mapping, the advantage being that it allows to compress the information, to accentuate a multispectral image and to isolate noise (Sheikhrahimi et al., 2019; Beygi et al., 2021). A significant number of studies have achieved lithological discrimination, by applying the PCA method on ASTER data, in order to enhance rock boundaries (Othman & Gloaguen, 2017; Bentahar & Raji, 2021).

The nine ASTER spectral bands available are highly correlated with each other (Table 2). Their correlation coefficient ranks between 0.7 and 0.9 (Table 2), whereas the nine Principal Components (PCs) (Fig. 9) that were derived from the reflectance of ASTER data, are uncorrelated variables (Ge et al., 2018). The nine new PCs show a decrease in variance rate (Table 3). Hence, in an effort to enhance lineament extraction, we have selected the PC1

Table 2. Matrix of correlation index derived from PCA analysis of the nine ASTER bands.

Correlation	Band 1	Band 2	Band 3	Band 4	Band 5	Band 6	Band 7	Band 8	Band 9
Band 1	1.000								
Band 2	0.955	1.000							
Band 3	0.722	0.844	1.000						
Band 4	0.898	0.905	0.804	1.000					
Band 5	0.783	0.874	0.901	0.713	1.000				
Band 6	0.901	0.933	0.798	0.702	0.879	1.000			
Band 7	0.785	0.995	0.787	0.747	0.821	0.774	1.000		
Band 8	0.889	0.897	0.936	0.807	0.720	0.965	0.747	1.000	
Band 9	0.758	0.757	0.928	0.937	0.749	0.884	0.841	0.736	1.000

Table 3. Percentage of information contained in each PCA bands extracted from ASTER bands.

PC Layer	EigenValue	Percent of EigenValues	Accumulative of EigenValues
1	3831,94017	94,7659422	94,7659422
2	138,582775	3,42722659	98,1931688
3	63,870168	1,57954362	99,7727125
4	8,522163	0,21075768	99,9834701
5	0,312462	0,00772735	99,9911975
6	0,235643	0,00582758	99,9970251
7	0,059392	0,0014688	99,9984939
8	0,043017	0,00106383	99,9995577
9	0,017885	0,00044231	100

for lineament extraction, while the first three PCs bands (Fig. 10A) that account for about 99 per cent of the total ASTER data (Table 3) were selected for lithological discrimination.

4.2. Band ratio

In the present study, we have employed band ratio images to map rock units in the Amezri-Amassine area. This method improves the spectral differences and discrimination of rock types, by involving the use of particular bands (Traore et al., 2022). It is widely used to delineate minerals and rocks which are not seen in raw bands, by dividing the spectral value of one band by the represented value of another band (Ahmadi & Kalkan, 2021). The selected combinations of bands allow the distribution of absorption features and increase the contrast of certain spectral features of ground objects (Çörtük et al., 2020; Beygi et al., 2021). Moreover, it reduces the haze and effects of topography (Ge et al., 2018; Ahmadi & Kalkan, 2021; Beygi et al., 2021).

Colour band ratios are good in enhancing lithological features. Accordingly, by taking into account the absorption features of carbonate minerals, we have selected 4/6, 5/8 and 4/5 band ratios image (Fig. 10B), in order to distinguish lithological boundaries. This newly adopted band-ratio image was validated by using geological field data and previously published maps, as well as by calculating the levels of information redundancy (Table 2). The matrix of correlation index of Table 2 indicates that each band combination, selected to make the

Table 4. PCA eigen vector matrix in nine bands of ASTER image.

PC/ASTER bands	Band 1	Band 2	Band 3	Band 4	Band 5	Band 6	Band 7	Band 8	Band 9
PC 1	0.252	0.358	0.367	**0.450**	0.313	**–0.316**	0.348	0.302	–0.242
PC 2	–0.380	0.170	–0.502	0.274	**0.279**	0.263	0.229	**–0.519**	0.167
PC 3	–0.126	0.063	0.015	**0.503**	**–0.642**	0.098	0.192	–0.223	0.464
PC 4	–0.717	–0.140	0.663	0.106	–0.038	–0.012	–0.109	–0.025	0.005
PC 5	0.033	–0.092	–0.045	0.450	–0.595	–0.518	0.253	0.312	0.026
PC 6	0.486	–0.714	0.372	–0.054	–0.183	0.275	–0.027	–0.001	0.008
PC 7	0.030	0.080	–0.105	0.264	–0.228	0.121	–0.526	–0.242	0.712
PC 8	0.138	–0.225	0.135	–0.101	0.548	–0.678	0.022	–0.044	0.370
PC 9	0.055	–0.027	–0.030	0.090	0.182	–0.042	–0.658	0.683	–0.226

best independent band ratio, displays a low amount of duplication (low correlation index). In addition, the values of contribution of each band in each principal component (Table 4) lead also to the choice of these band ratios as the best ones derived from PC1, PC2 and PC3, respectively. PC1 displays reflectance in band 4, with a positive contribution (0.450), and absorption in band 6 with a negative contribution (–0.316). In the same way, the PC2 shows absorption in band 8, with a negative contribution (–0.519), and reflectance in band 5, with a positive contribution (0.279). In addition, PC3 shows reflectance in the same band as PC1, with a positive contribution (0.503), and absorption in band 5, having a negative contribution (–0.642). These differing contributions justify the capability of this composite image (Fig. 10B) to highlight the differences between various geological bodies.

4.3. Minimum Noise Fraction

MNF is another technique of reducing data dimensions into smaller numbers of components, and converting correlated variables into independent components (Malainine et al.,2021; Morsli et al., 2021). The MNF transformation was developed to generate new components and determine the inherent dimensionality of data processed (Ge et al., 2018; Shirmard et al., 2020).

Many previous studies have used the classic MNF transform in order to isolate and segregate noise from signal in the ASTER data set (Ge et al., 2018; Çörtük et al., 2020; Shirmard et al., 2020). MNF technique was used by Shirmard et al. (2020) for highlighting hydrothermal alteration zones in the Toroud-Chahshir arc (central Iran). In addition, Traore et al.(2022) have recently showed the effectiveness of the MNF method for discriminating carbonate-hosted Pb-Zn mineralisations in the eastern Taurus (Turkey). Other studies have previously shown great potential in mapping lithological units (Muavhi & Mavhungu, 2020; Garain et al., 2021; Malainine et al., 2021; Morsli et al., 2021).

MNF technique has been implemented in the present work with a view to improve the visual interpretation, which increases the possibilities for delineating rock units and extracting useful geological information. MNF was already applied on ASTER images (VNIR-SWIR bands) by several authors (Çörtük et al., 2020). We have selected the first MNF Bands (MNF1, MNF2 and MNF3) (Fig. 11) in order to construct an MNF RGB image (Fig. 10C), because they involved the lowest noise with highest eigen values (Table 5).

4.4. Directional filter

Many past studies display the effectiveness of directional filtering for highlighting specific linear features, using ASTER images (Khodadadi & Arfania, 2017; Sheikhrahimi et al., 2019; Muavhi & Mavhungu, 2020; Bentahar & Raji, 2021). Directional filtering is a spatial domain filtering technique that convolves the extraction of gradient and edges, corresponding to structural or lithological discontinuities (Muavhi & Mavhungu, 2020). The filtering algorithm produces the first difference of the image input in all directions. In the basic, the directional filter is made up of two kernels with two arrays of 3 × 3 pixels (van Andel, 1998). The left array is multiplied by cosα while the right array is multiplied by sin α; α refers to the angle, between the north and the linear direction, to be highlighted (Pour & Hashim, 2015). In the northeast quadrant, angles are considered negative, while they are positive in the northwest quadrant.

At this stage, the initial input was the PC1 image (Fig. 9), as obtained from the ASTER multispectral data. This principal component is highly relevant for identifying structural lineaments because it shows high contrast and resolution. It has been used by several authors to extract lineaments (Khodada-

Table 5. Percentage of information contained in each MNF bands extracted from ASTER bands.

MNFs	EigenValue	Percent of EigenValues	Accumulative of EigenValues
MNF1	926,406104	68,47396480	68,4739648
MNF2	190,179904	14,05687200	82,5308368
MNF3	142,410269	10,52604870	93,0568855
MNF4	27,953627	2,06615183	95,1230373
MNF5	23,909610	1,76724418	96,8902815
MNF6	13,900880	1,02746340	97,9177449
MNF7	11,430487	0,84486788	98,7626128
MNF8	10,350971	0,76507702	99,5276898
MNF9	6,390035	0,47231018	100

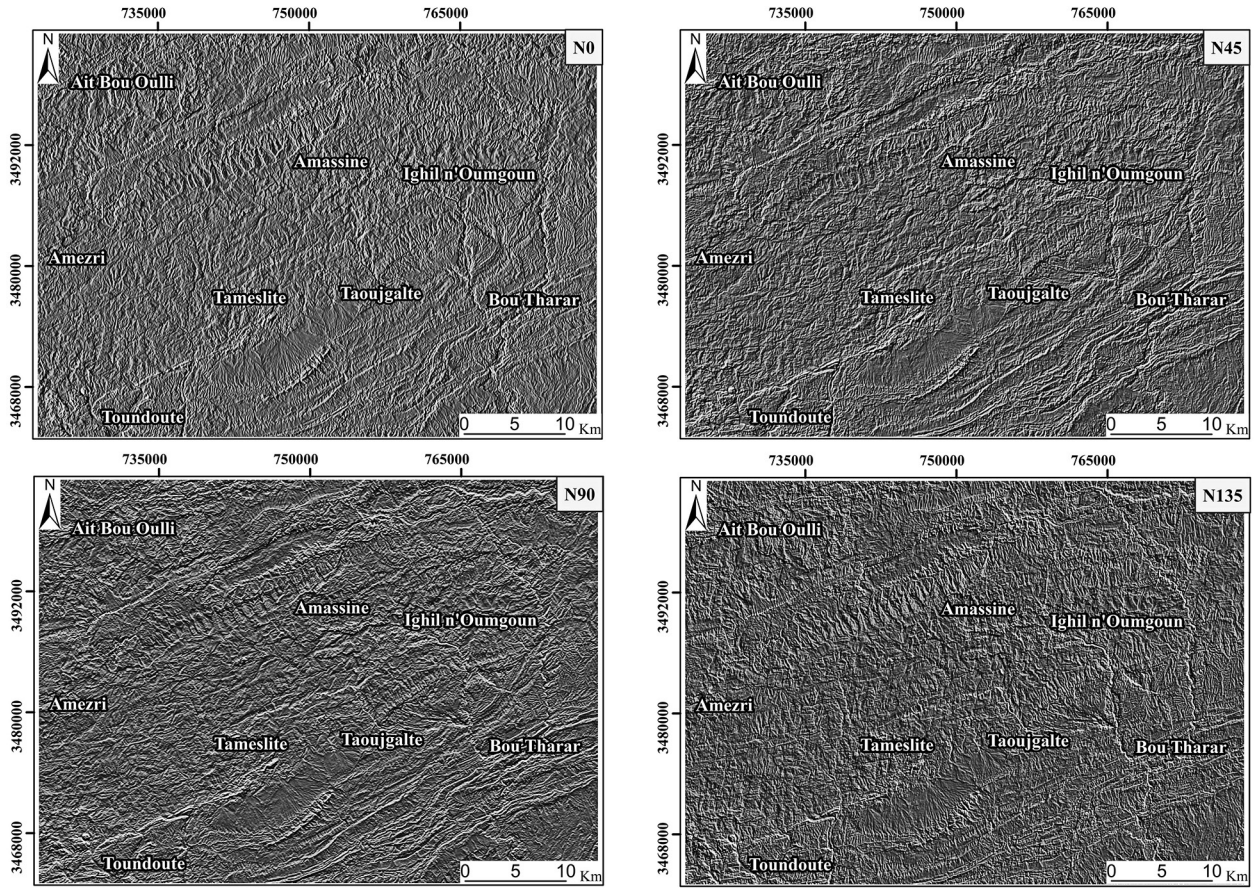

Fig. 6. Four subset-filtered images derived from PC1 image of ASTER.

di & Arfania, 2017). After that, the PC1 image underwent the directional convolution filtering to produce new images (Fig. 6), which accurately display edge contrast within the study area.

4.5. Shading relief

The shading relief is often used in order to extract lineaments from DEM data (Khodadadi & Arfania, 2017). It is used as a powerful tool for easy recognition of lineaments and to enhance lineament mapping, particularly in mountainous areas.

In the present study, four separate shaded relief images were constructed from the ASTER GDEM data, by maintaining a sun elevation angle at 30°. These incoming images (Fig. 7) were generated, with four contrasting illumination directions: N0°, N45°, N90° and N135°, by applying the analytical hill-shading tool of the ArcGIS software. This tool allows viewing terrain features at all angles by producing reflectance maps (Masoud & Koike, 2006). These maps are created by converting slope values to a reflectance value by using equation 1 of (Horn, 1981):

$$R(p, q) = \frac{1}{2} + \frac{\frac{1}{2}(p' + a)}{\sqrt{b^2 + (p' + a)^2}} \qquad \text{(eq. 1)}$$

$$p' = \frac{(p_0 q + q_0 q)}{\sqrt{(p_0^2 + q_0^2)}} \qquad \text{(eq. 2)}$$

where:

$$p = \frac{(z_9 + z_8 + z_7) - (z_3 + z_2 + z_1)}{8d}$$

$$q = \frac{(z_9 + z_6 + z_3) - (z_7 + z_4 + z_1)}{8d}$$

Z_i is the height at the location i (Fig. 8); d is distance between pixel centre;
$p_0 = 1/\sqrt{2}$ and $q_0 = -1/\sqrt{2}$; a and b are parameters allowing to control grey value intensity of horizontal continuous surfaces. Horn (1981) recommended $a = 0$ and $b = 1/\sqrt{2}$.

According to Bentahar et al. (2020) and Farah et al. (2021), the boundaries between the shaded and unshaded ground areas show the presence of lineaments.

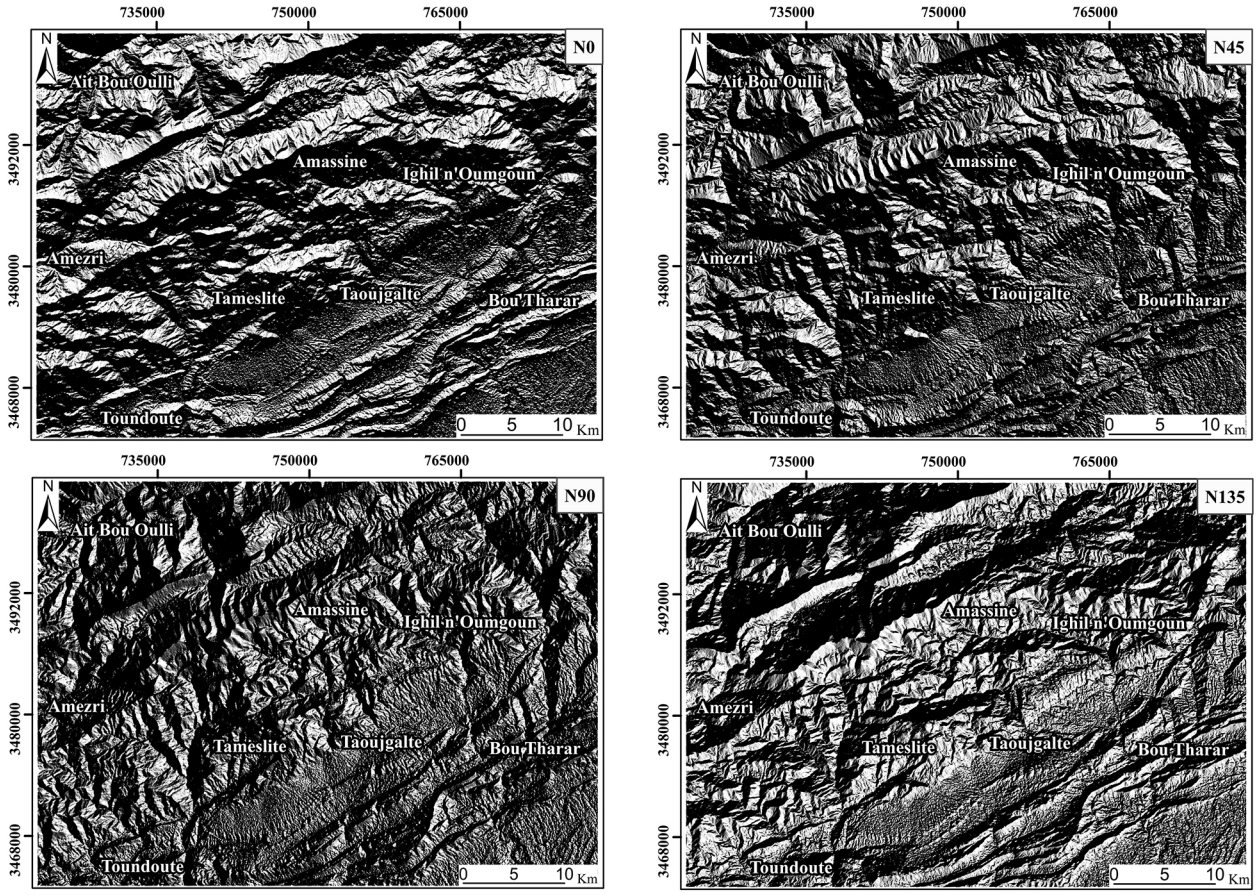

Fig. 7. Four shaded relief images generated from DEM ASTER.

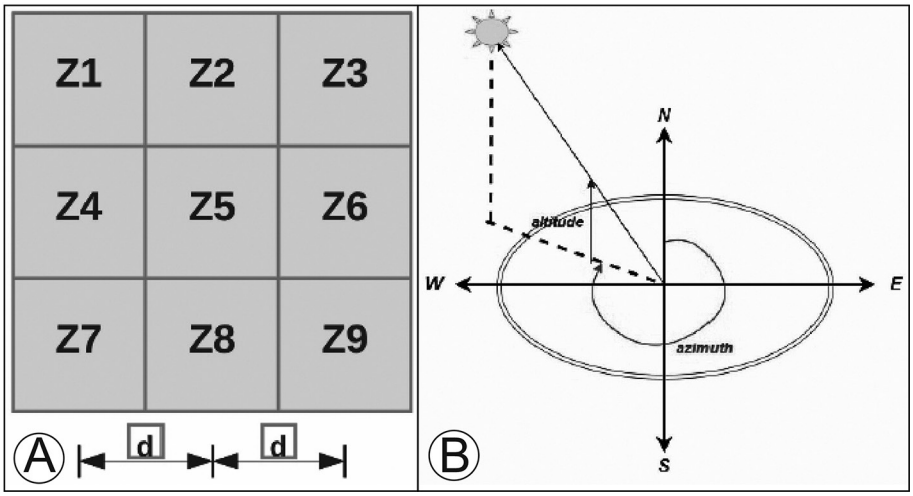

Fig. 8. A – 3 × 3 cell window representation of a surface; **B –**Illustration of light source altitude (45°) and azimuth (315°) angles (from Syzdykbayev et al., 2020).

4.6. Automatic lineaments extraction

In the present work, automated lineament extraction was applied by using the "LINE MODULE" algorithm of PCI Geomatica version 2013 software. This LINE module allows the extraction of linear features from images using six parameters (Table 6). According to www.pcigeomatics.com, these parameters include: RADI specifies the radius (in pixels) that will be used in the edge detection process. The lower values of this parameter allow the detection of more details, while the high values

Table 6. Parameter values used in the present work.

Parameters applied	Values
RADI (filter radius)	20
GTHR (Edge Gradient Threshold)	65
LTHR (Curve Length Threshold)	30
FTHR (Line Fitting Threshold)	5
ATHR (Angular Difference Threshold)	35
DTHR (Linking Distance Threshold)	25

are recommended to minimise noise detection. This parameter roughly defines the small detail in the processed image to be detected. Values between 3 and 8 are acceptable. GTHR (Gradient threshold) specifies the threshold of brightness change. It is defined as a minimum value of gradient that can be considered as an edge, during edge detection. LTHR (Length threshold) expounds the minimum length of the curve (in pixels), used for mapping curved and linear objects, which are taken as linear feature for further consideration. A value of 10 is suitable. FTHR (Line fitting error threshold) specifies the tolerance allowed when fitting arc or line segment to form a (curved) lineament. Values between 2 and 5 are ideal. ATHR (Angular difference threshold) indicates the maximum angle, not to be exceeded, between two neighbouring vectors to be linked. Values between 3 and 20 are recommended. DTHR (Linking distance threshold) defines the maximum distance between the endpoints of a polyline, to be linked. Values between 10 and 45 are suitable.

At this stage, the input data were the four directional filters (Fig. 6) and the four shaded reliefs (Fig. 7) created from derivatives of ASTER data. Subsequently, different values of parameters were tested, and the most suitable were selected (Table 6) in order to obtain the most significant lineaments. Consequently, two lineament maps (Figs. 12, 13) are derived after removing non-geological lineaments.

5. Results and discussion

5.1. Lithological mapping

In the present study, three methods (PCA, BR and MNF) were examined to discriminate rock units within the Amezri-Amassine area, in detail. Each method shows its effectiveness; but the MNF technique, already proposed, was found to be the most effective method. As shown in Figure 2, the rock units of the Amezri-Amassine area are well exposed and rarely covered by vegetation. Moreover, the boundaries between them are clear, and not masked by weathering, which make the target area an ideal field for remote sensing studies.

The resulting images of PCA analysis show that the Principal components 4, 5, 6, 7, 8 and 9 (Fig. 9) are devoid of any desired information, related to mapping minerals. In addition, they display a constant decrease in quality from the PC1 image to the last one. As the first three components synthesize around 99.8 per cent of the information contained in the original image (Table 3), these three components seem indispensable. Components 4–9 each contain a low amount of information, less than 0.21 per cent and appear unnecessary (Table 3). In this sense, only the first three principal components are used in the present work. The first three principal component image (Fig. 10A) displays a good visualization of several lithological units. This PCA composite image visualizes and improves the separation of some spectral lithological units, in the study area. This is explained by the high amount of information carried by this image from all bands; PC1, PC2 and PC3 contain high variance of original data (Table 3). This reason was already mentioned and discussed by several authors (Çörtük et al., 2020; Eldosouky et al., 2021). The basaltic rocks and shales (Fig. 14A, C) have been reliably delineated by this image. However, it is difficult to separate between the Lower Jurassic carbonate in the Amezri-Amassine area and carbonate formations dated as Cretaceous and Eocene, which appear in a lime colour (limestone in Fig. 10A). Therefore, this specialized image, of ASTER data, proposed, does not allow separating Triassic pelites and sandstones from Precambrian flysch rocks. These two formations are both displayed in a sky-blue colour (Fig. 10A, south of Amezri).

Regarding the results of fieldwork in the study area (Fig. 14), gypsum-bearing rocks (Fig. 14B) are often associated with detrital sedimentary rocks, including the argillaceous and siltstone strata. However, gypsum formation appears as orange shade (Fig. 10A), which impedes its visibility within the gypsum-limestone complex. Hence, it is necessary to implement another method that may offer accurate separation of lithological units in the study area. The band ratio combinations of 4/6, 5/8 and 4/5 have been generated in order to highlight the local lithological formations. This method is effective to highlight certain features that cannot be emphasised apparently in a single band (Ge et al., 2018). Several band ratios were assessed; the selected ones are the most effective ratios to produce a colour combination image. The band ratios 4/6 and 5/8 were selected because of their ability to

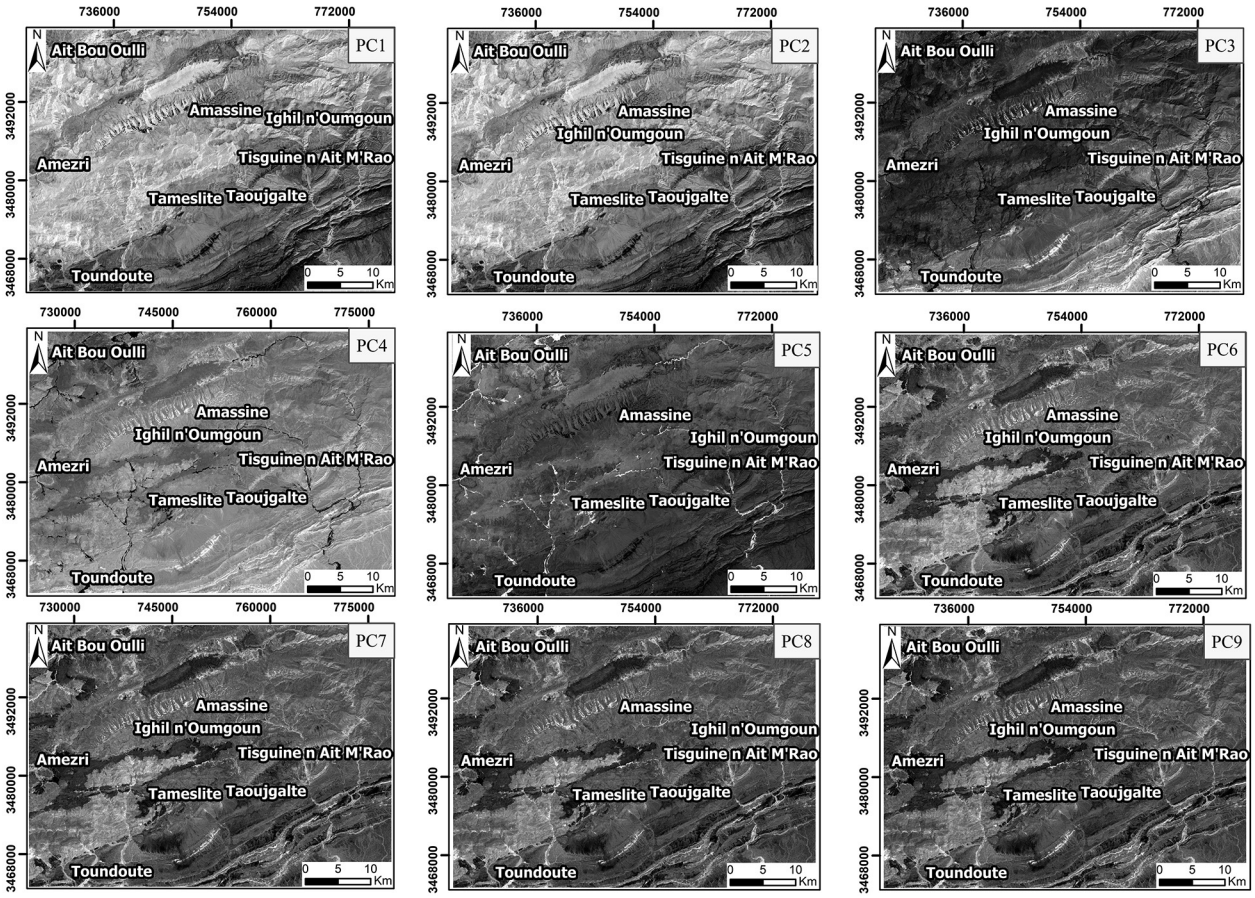

Fig. 9. PCA images of SWIR and VNIR ASTER data.

identify muscovite/illite and calcite, respectively (Sheikhrahimi et al., 2019).

As illustrated in Figure 10B, the band ratio image highlights Palaeozoic shales in mint colour and Precambrian flysch in crepe hue (northwestern part of Toundoute). In addition, results show that carbonate rocks, depicted in dark pistachio, are the most extensive formation in the Amezri-Amassine area, which are commonly associated with Triassic red-bed deposits (clays with gypsum layers displayed in fuchsia colour). However, Miocene-Pliocene rocks are poorly discriminated from the detrital formations of Pleistocene-Holocene age, in complicated mixed colours (ochre and carrot colours), at the southeastern part of the study area. Moreover, in this band ratio image, Triassic basalts, which are mostly observable in the field associated with siliciclastic deposits (Fig. 14A), display a colour (mint colour) similar to the Cambro-Ordovician adjacent shales (Fig. 14C), south of Amezri. As the PCA image, this image does not show the capability either to separate the gypsum rocks from other rock units.

The MNF transformation was also implemented in the present work. This method is essential to highlight certain ground objects that cannot be emphasized seemingly in band ratio and PCA images. The analysis of the MNF method applied to ASTER data shows the capability of the former to identify lithological units. The nine resulting MNF components (Fig. 11) display the degradation of information towards the last MNF components. In addition, the last six MNF components are devoid of any useful information, while the first three carry a high amount of information (Table 5). These three MNF components are shown in Figure 10C, as an RGB image.

The resulting image distinguishes basaltic rocks from detrital formations (Fig. 14A), in red fox colour, and highlights limestone rocks (Fig. 14B) within the Jurassic formation, in lime to pear colours. As verified in the field, a sky blue tone is attributed to Eocene conglomerates (Fig. 14D), whereas the upper Miocene siliciclastic rocks (clays with gypsum) are depicted in purple. Within the Palaeozoic deposits, the Cambrian flysch and Ordovician shales (Fig. 14C) manifest brown and grape colours, respectively, north of Toundoute. The Paleocene to Pleistocene rocks (lacustrine limestone and sandy

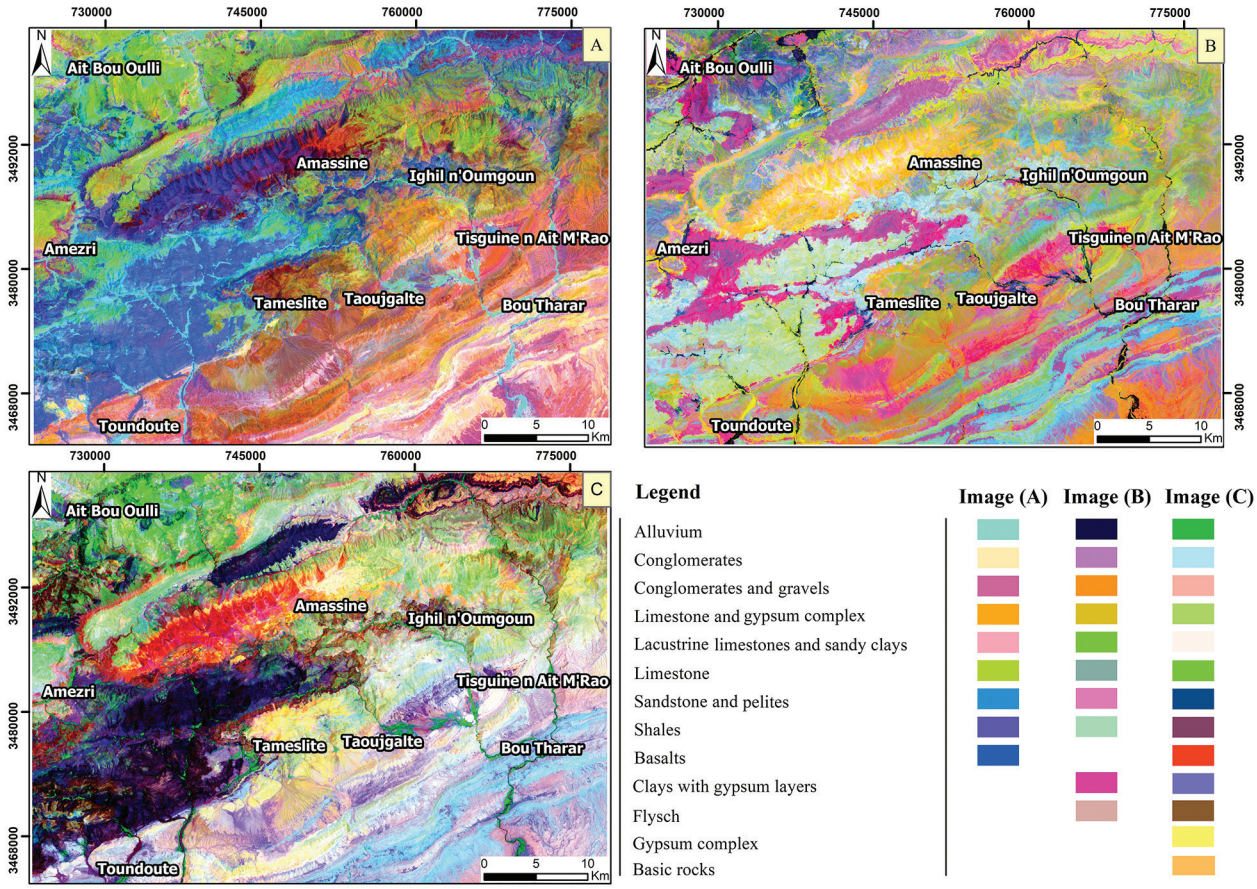

Fig. 10. A – PC1, PC2, PC3 RGB colour combination image derived from ASTER image; **B –** 4/6, 5/8 ,4/5 RGB colour composite, of ASTER image; **C –**MNF1, MNF2, MNF3 RGB colour combination image.

clay) appear as pink carnation to flamingo hue. This image has also the advantage of highlighting the siliciclastic deposits (sandstones and pelites) and basaltic intrusion (Fig. 14D), attributed to the Middle Jurassic, in dark blue and royal orange, respectively, in the northern part of the study area.

As verified in the Amezri-Amassine field, the Lower Liassic carbonates of this region are overlain by gypsum and siltstone layers (Fig. 14B) that are not observable on the geological map (Fig. 2). For instance, Figure 10C results from the MNF method, as used in previous studies (Muavhi & Mavhungu, 2020; Shirmard et al., 2020; Garain et al., 2021; Malainine et al., 2021; Morsli et al., 2021; Traoreet al., 2022), not only delineates the occurrence of carbonates and clay rocks in the Amezri-Amassine district, but also separates accurately gypsum and siltstone formations from surrounding rocks in yellow hue. Comparing the results of the present study with field data (Fig. 14) show the effectiveness of the image processing algorithms used, to highlight certain formations that are absent from the geological map (Fig. 2). Moreover, the MNF transformation was found to be the more efficient technique to highlight all lithological units, with high colour contrast, as well as more clear-cut boundaries.

5.2. Lineament mapping

From the ASTER images processed, about 4,580 geological lineaments were extracted, by applying the automatic method. However, many insignificant lineaments of anthropogenic origin were also detected. In order to eliminate lineaments of anthropogenic origin (road, track, rail bitumen and electric grids), all the extracted lineaments were systematically checked; by overlaying them on topographic and geological maps using GIS tools. In addition, the superposition of the lineament pattern and the ASTER GDEM map of the study area allowed to detect and remove linear structures, derived from hydrographic network (valley bottoms) and false hits (ridge line, shade, etc.). The lineaments corresponding to the contacts of rock units (Fig. 14E, F) were also eliminated. This post-processing step assured to extract only linear features caused by faulting. However, many lineaments, related to ridge line

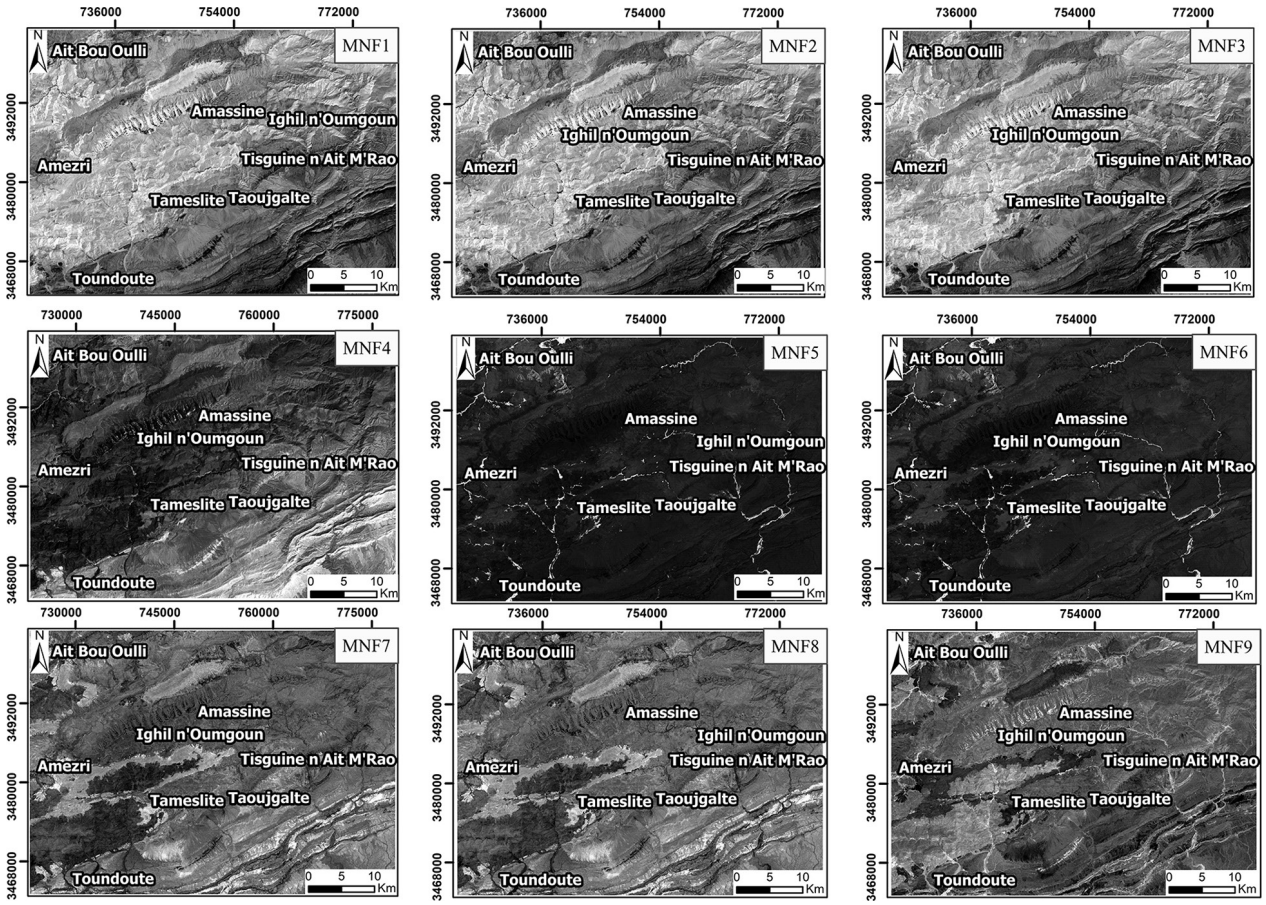

Fig. 11. MNF images of SWIR and VNIR ASTER data.

and to hydrographic pattern, may be controlled by faults. Likewise, roads and other man-made constructions follow rivers and topography. Accordingly, in order to discriminate lineaments caused by faulting from others, the validation of tectonic lineaments has been supported by geological maps, regional palaeostress fields, structural data and field work (Fig. 14).

After discarding non-structural lineaments, the remainder of lineaments extracted from PC1 ASTER image and ASTER GDEM data, in four directions, were merged to form two composite lineament maps. The two lineament maps elaborated, and their statistical analysis, are displayed in Figures 12 and 13.

The PC1ASTER image and ASTER GDEM image yielded a large number of lineaments in the order of 2,118 and 2,284, respectively. The length frequency diagram of the PC1 ASTER image shows that the length of the lineaments identified is between 0.9 and 11.6 km, while Figure 12B shows that the length of the majority of lineaments, in the ASTER GDEM image, is between 0.8 and 15.8 km. On the lineament map, derived from ASTER GDEM image, some lineaments show small extents. Nevertheless, most of them are located near existing faults. In turn, the results obtained from the PC1 image display a better correlation with the distribution of the main faults in the field (Fig. 12A). In fact, the irregular pattern, on both lineament maps, reflects the high effect of faulting processes in the study area. The high concentration of lineaments appeared near the highly fractured zones (Figs. 12, 13). Some examples of faults and geological lineaments, which were checked and validated in the Amezri-Amassine area by field work, are displayed in Figure 14G, H and I.

The rose diagram of the lineaments extracted from GDEM image clearly indicates two major directions, i.e., WSW-ENE and W-E (Fig. 13D). With respect of regional tectonics, this map validates the trends of faults already shown on the geological map and shows the presence of another linear structures which differ in orientation from the fault pattern. These subordinate structures are located in north of Amassine, with a NW-SE direction. For the PC1 data, the extracted lineaments show one dominant direction of WSW-ENE (Fig. 12D). Except for the trend newly detected, the trends of all lineaments extracted in the present work corre-

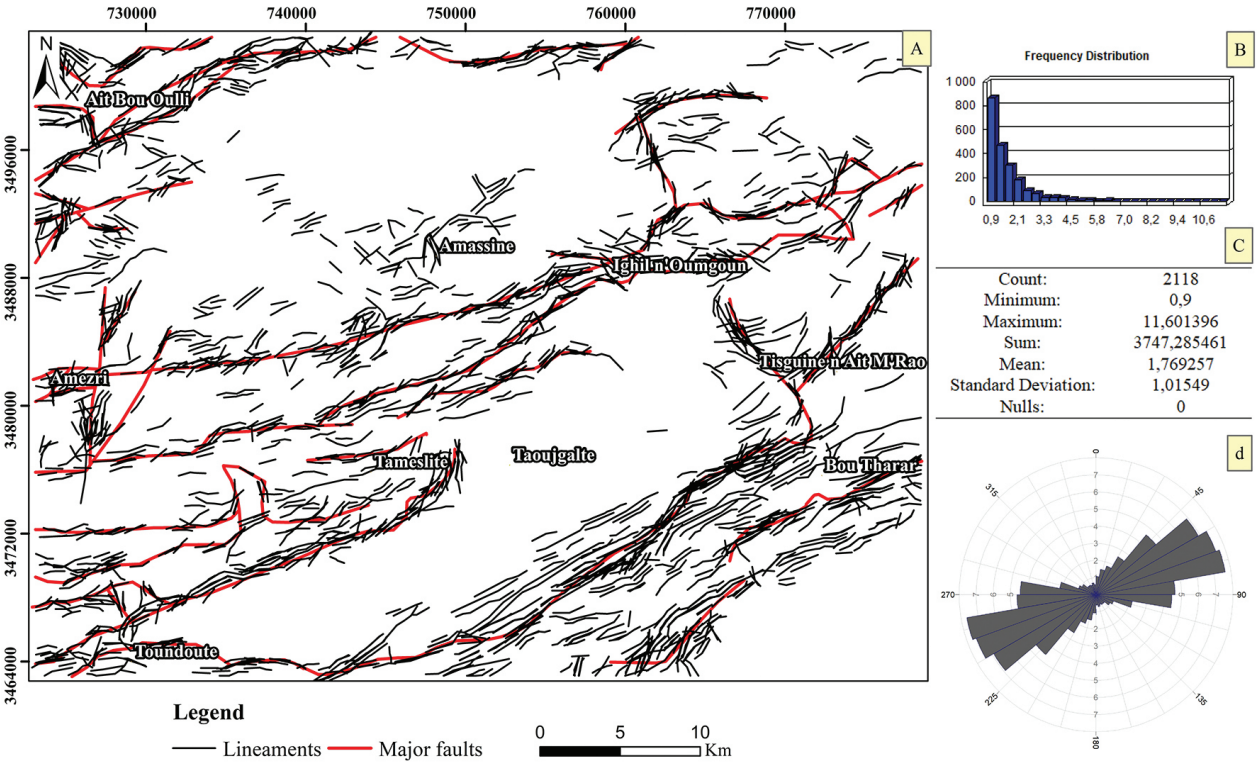

Fig. 12. A –Synthetic lineament maps derived from PC1 image after elimination of non-geological lineaments; B – Length frequency diagram of lineaments; C – Basic statistics of lineaments extracted; D – Rose diagram of lineaments extracted.

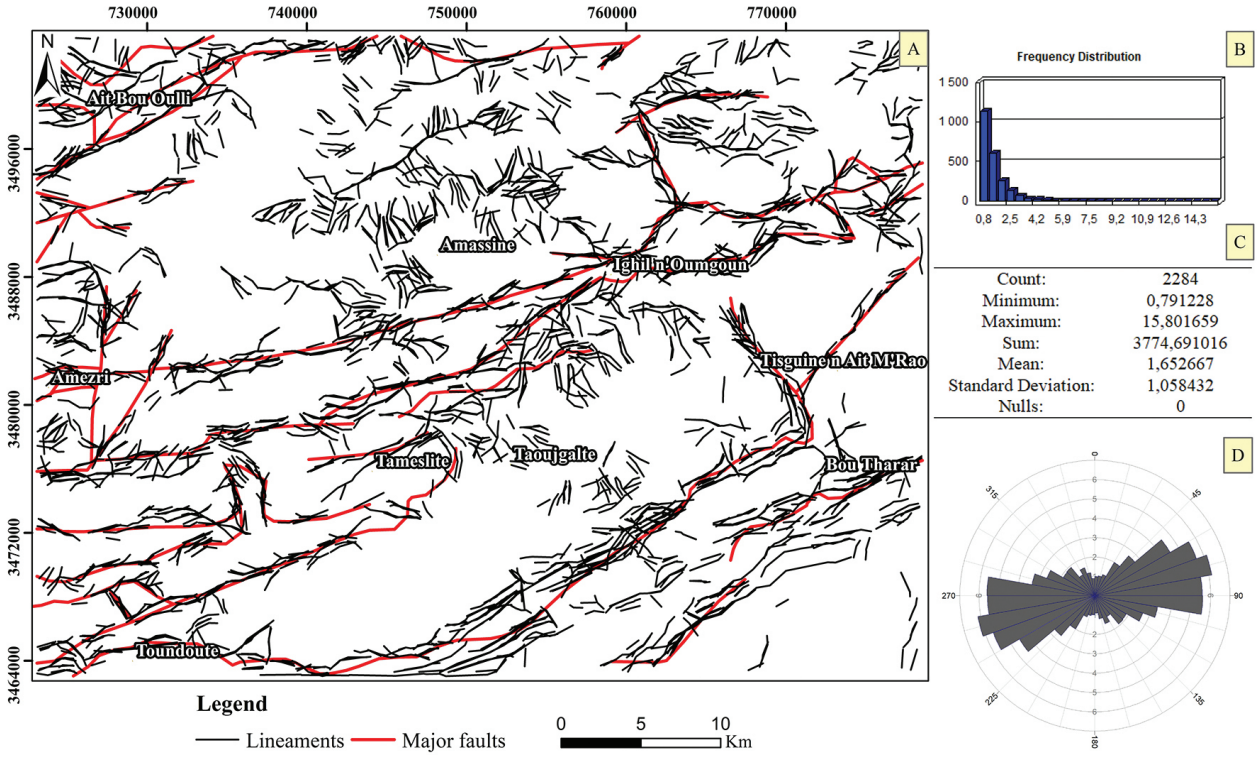

Fig. 13. A –Synthetic lineament maps from GDEM ASTER image (30 m of resolution) after elimination of non-geological lineaments; B – Length frequency diagram of lineaments; C –Basic statistics of lineaments extracted; D – Rose diagram of lineaments.

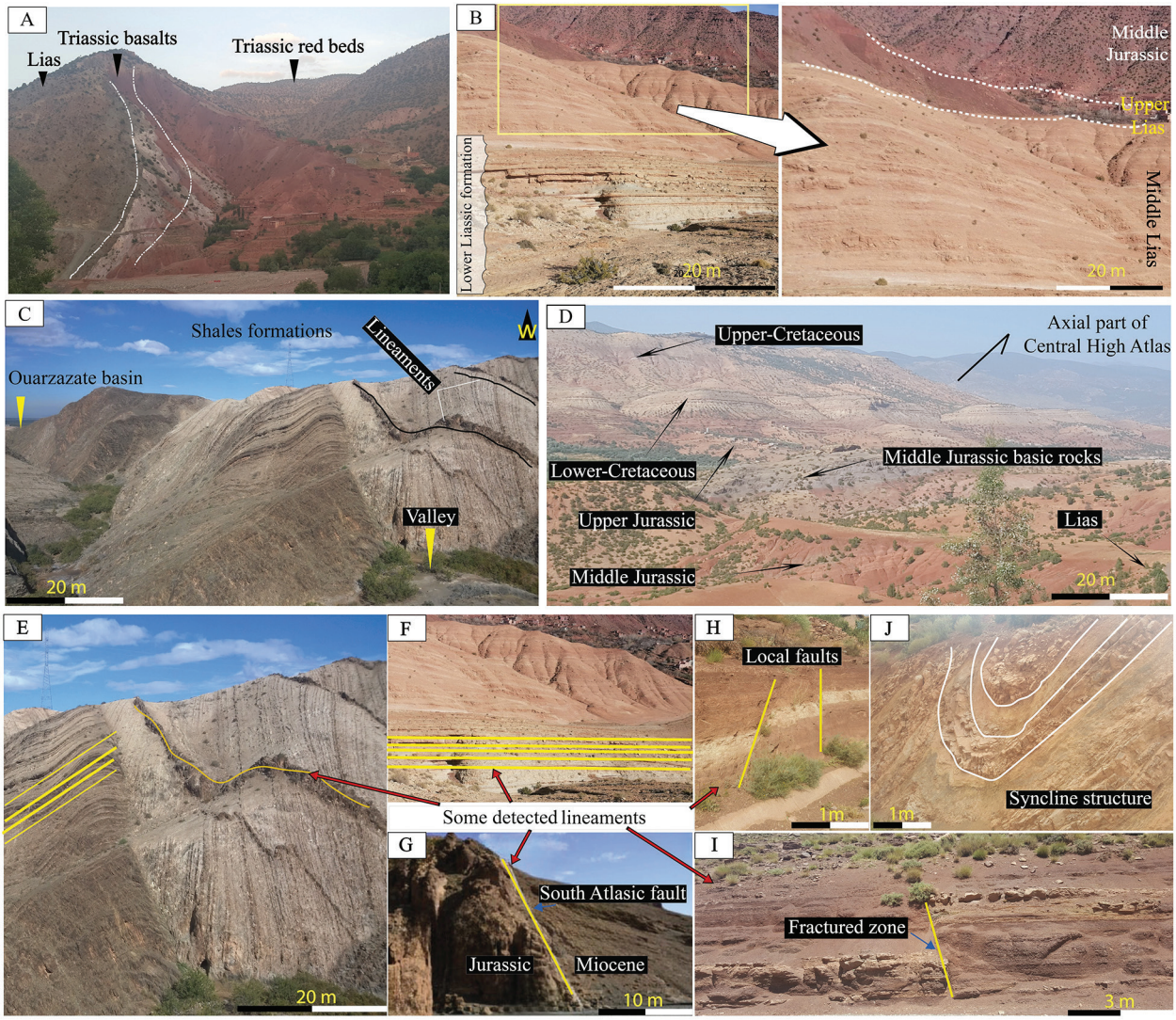

Fig. 14. A-D – Field photographs of some lithological units identified; E-J – Field photographs of certain geological lineaments, including structural and non-structural lineaments. The locations of all photographs are displayed in Figure 2.

spond perfectly to the major faults, recognised on the structural map of the Amezri-Amassine area (Michard et al., 2008), which confirms the tectonic impact of Mesozoic events in this region. However, the W-E trend correspond to the trend of the fault boundaries of the belt, like the south Atlasic fault (Fig. 14G) (Schwarz & Wigger, 1988), which is assumed to be a deep-reaching fault system and considered a long-lived Hercynian transcurrent thrust (Michard et al., 2008).

Within the NE-SW fault zone, Riedel fractures have been previously described by Domènech et al. (2015), suggesting a certain component of sinistral strike-slip during the Triassic transtensional stress field. Sinistral fractures with a N40 direction and dextral faults with a N10 direction are both recognised within these fault zones (Sintubin et al., 1997). However, during Meso-Cenozoic times these faults were reactived in reverse faults due to the transpressional stress field. For the NW-SE structural lineament, newly detected by the present study, they have been already distinguished within the Triassic and Jurassic rocks of the eastern High Atlas where it is considered as the recent family of faults that cut in right-lateral play the W-E faults (Himyari et al., 2001).

However, the adopted method does not allow highlighting the folds axes, which are abundant in the CHA. Figure 14J shows an example of giant syncline which was not detected by the present study. This failure is probably due to the effect of vegetation as a parameter that masks the structural data of this region. In the end, we conclude that the newly adopted automatic extraction analysis contributes fully to precisely extract lineaments here.

6. Conclusions

The area under investigation exhibits a wide variety of rocks, displaying different lithological characteristics, and ranging in age from Precambrian to Quaternary. The present study aims to evaluate, for the first time, the potential of ASTER data in the discrimination of lithological units and in lineament mapping by applying several enhancement techniques. The image processing methods used here, such as PCA, BR and MNF, have proved their capability to enhance the quality of multispectral ASTER images for lithological mapping. The appropriate band ratio image, which allows differentiating different rock units and highlighting lithological boundaries, was selected by analysing several combinations of bands ratios. The MNF image also shows good results with less noise, higher colour contrast and increased accuracy, in separating and highlighting new rock units. In addition, these results confirm the efficiency of the MNF method in terms of discriminating carbonates and gypsum-bearing rocks. The followed approach allowed the characterisation of different rock types including, basaltic rocks, metamorphic basement rocks, as well as siliciclastic and carbonate sedimentary rocks.

The present study also assesses the contribution of ASTER GDEM and GIS techniques to mapping lineaments. The ASTER data have proved to be powerful for extracting lineaments, by using the directional filter, which provides a high accuracy in analyses of geological structures. The results display a large number of tectonic lineaments that present consistent variations, in length and trend, with a predominance of WSW-ENE and W-E directions. In addition, a new family of faults, trending in a NW-SE direction, has been discovered in this region.

The validation of results obtained by using a previously published geological map, coupled with field observations, indicate the capability of the envisaged ASTER data, and their potential to update the existing geological map. Furthermore, the ASTER data highlight the usefulness of MNF transformation PCA method and newly proposed ASTER band-ratio image, for lithological mapping in the Amezri-Amassine area.

Finally, the ASTER data processing method proposed can be used as a rapid, powerful and cost-effective tool for mapping areas, particularly under the same atmospheric conditions around the world. In the near future, we plan to evaluate the potential of the Landsat-8 OLI and Sentinel sensors in comparison with the ASTER sensor, in lithological mapping, by using supervised classifications.

Acknowledgements

The authors would like to thank the NASA-USGS GLOVIS-GATE for the satellite data (ASTER L1B image), and the http://glovis.usgs.gov// for the ASTER GDEM data. The authors are also very grateful to the anonymous reviewers for their valuable comments and suggestions and to the journal editor for careful review of the article.

References

Adiri, Z., El Harti, A., Jellouli, A., Lhissou, R., Maacha, L., Azmi, M., Zouhair, M. & Bachaoui, E.M., 2017. Comparison of Landsat-8, ASTER and Sentinel 1 satellite remote sensing data in automatic lineaments extraction: A case study of Sidi Flah-Bouskour inlier, Moroccan Anti Atlas. *Advances in Space Research* 60, 2355–2367.

Ahmadi, H. & Kalkan, K., 2021. Mapping of Ophiolitic Complex in Logar and surrounding areas (SE Afghanistan) with ASTER data. *Journal of the Indian Society of Remote Sensing* 49, 1271–1284.

Ait Addi, A. & Chafiki, D., 2013. Sedimentary evolution and palaeogeography of mid-Jurassic deposits of the Central High Atlas, Morocco. *Journal of African Earth Sciences* 84, 54–69.

Amer, R., El Mezayen, A. & Hasanein, M., 2016. ASTER spectral analysis for alteration minerals associated with gold mineralization. *Ore Geology Reviews* 75, 239–251.

Benammi, M. & Toto, E.A., 2005. Tectonique tangentielle Atlasique dans les bassins synorogeniques Neogenes de Ourzazate et D'aït Kandoula (bordure sud du Haut Atlas, Central Maroc). *Revista de la Sociedad Geológica de España* 18, 151–162.

Benammi, M., Arbi Toto, E. & Chakiri, S., 2001. Les chevauchements frontaux du Haut Atlas central marocain : styles structuraux et taux de raccourcissement différentiel entre les versants nord et sud. *Comptes Rendus de l'Académie des Sciences – Series IIA – Earth and Planetary Science* 333, 241–247.

Bentahar, I. & Raji, M., 2021. Comparison of Landsat OLI, ASTER, and Sentinel 2A data in lithological mapping : A case study of Rich area (Central High Atlas, Morocco). *Advances in Space Research* 67, 945–963.

Bentahar, I., Raji, M. & Si Mhamdi, H., 2020. Fracture network mapping using Landsat-8 OLI, Sentinel-2A, ASTER, and ASTER-GDEM data, in the Rich area (Central High Atlas, Morocco). *Arabian Journal of Geosciences* 13, 768.

Beygi, S., Talovina, I.V., Tadayon, M. & Pour, A.B., 2021. Alteration and structural features mapping in Kacho-Mesqal zone, Central Iran using ASTER remote sensing data for porphyry copper exploration.

International Journal of Image and Data Fusion 12, 155–175.

Çörtük, R.M., Çelik, Ö.F., Alkan, A., Özkan, M. & Özyavaş, A., 2020. Distribution of rocks in Pınarbaşı Ophiolite from central Anatolia (Turkey) based on analysis of ASTER and Landsat-8 data. *Geological Journal* 55, 6810–6822.

De Jong, C., Cappy, S., Finckh, M. & Funk, D., 2008. A transdisciplinary analysis of water problems in the mountainous karst areas of Morocco. *Engineering Geology* 99, 228–238.

Domènech, M., Teixell, A., Babault, J. & Arboleya, M.-L., 2015. The inverted Triassic rift of the Marrakech High Atlas: A reappraisal of basin geometries and faulting histories. *Tectonophysics* 663, 177–191.

Eldosouky, A.M., El-Qassas, R.A.Y., Pour, A.B., Mohamed, H. & Sekandari, M., 2021. Integration of ASTER satellite imagery and 3D inversion of aeromagnetic data for deep mineral exploration. *Advances in Space Research* 68, 3641–3662.

Ellero, A., Malusà, M.G., Ottria, G., Ouanaimi, H. & Froitzheim, N., 2020. Transpressional structuring of the High Atlas belt, Morocco. *Journal of Structural Geology* 135, 104021.

Ettachfini, E.M., Souhel, A., Andreu, B. & Caron, M., 2005. La limite Cénomanien-Turonien dans le Haut Atlas central, Maroc. *Geobios* 38, 57–68.

Farah, A., Algouti, Ahmed, Algouti, Abdellah, El badaoui, K., Errami, M. & Ifkirne, M., 2021. *Lithological mapping and automatic lineament extraction using ASTER and Gdem data in the Imini-Ounilla-Asfalou district, South High Atlas of Marrakech, Morocco*. E3S Web Conference 240, 04002.

Garain, S., Mitra, D. & Das, P., 2021. Mapping hydrocarbon microseepage prospect areas by integrated studies of ASTER processing, geochemistry and geophysical surveys in Assam-Arakan Fold Belt, NE India. *International Journal of Applied Earth Observation and Geoinformation* 102, 102432.

Ge, W., Cheng, Q., Jing, L., Armenakis, C. & Ding, H., 2018. Lithological discrimination using ASTER and Sentinel-2A in the Shibanjing ophiolite complex of Beishan orogenic in Inner Mongolia, China. *Advances in Space Research* 62, 1702–1716.

Hewson, R., Robson, D., Carlton, A. & Gilmore, P., 2017. Geological application of ASTER remote sensing within sparsely outcropping terrain, Central New South Wales, Australia. *Cogent Geoscience* 3, 1319259.

Himyari, S.M., Hoepffner, C. & Benzakour, M., 2001. Étude structurale du Haut Atlas Oriental (Maroc) à l'aide de l'analyse linéamentaire des images HRV (XS) de SPOT 2. *Contemporary Publishing International Télédétection* 2, 243–253.

Horn, B.K.P., 1981. Hill shading and the reflectance map. *Proceedings of Institute of Electrical and Electronics Engineers* 69, 14–47.

Hunt, G.R., 1977. Spectral signatures of particulate minerals in the visible and near infrared. *Geophysics* 42, 501–513.

Imran, M., Ahmad, S., Sattar, A. & Tariq, A., 2022. Mapping sequences and mineral deposits in poorly exposed lithologies of inaccessible regions in Azad Jammu and Kashmir using SVM with ASTER satellite data. *Arabian Journal of Geosciences* 15, 538.

Jacobshagen, V., Brede, R., Hauptmann, M., Heinitz, W. & Zylka, R., 1988. Structure and post-Palaeozoic evolution of the central High Atlas. [In:] Jacobshagen, V.H. (Ed.), The Atlas System of Morocco, Lecture Notes in Earth Sciences. Springer-Verlag, Berlin, pp. 245–271.

Khodadadi, F. & Arfania, R., 2017. Alteration mapping in central Urumieh-Dokhtar Magmatic Assemblage of Iran using ASTER and OLI data. *Open Journal of Geology* 07, 1215–1226.

Laville, E. & Piqué, A., 1992. Jurassic penetrative deformation and Cenozoic uplift in the Central High Atlas (Morocco): A tectonic model. structural and orogenic inversions. *Geologische Rundschau von Stuttgart* 81, 157–170.

Malainine, C.-E., Raji, O., Ouabid, M., Khouakhi, A., Bodinier, J.-L., Laamrani, A., El Messbahi, H., Youbi, N. & Boumehdi, M.A., 2021. An integrated ASTER-based approach for mapping carbonatite and iron oxide-apatite deposits. *Geocarto International* 37, 6579–6606.

Marzoqi, M. & Pascal, A., 2000. Séquences de dépôts et tectono-eustatisme à la limite Crétacé/Tertiaire sur la marge sud-téthysienne (Atlas de Marrakech et bassin de Ouarzazate, Maroc). *Newsletters on Stratigraphy* 38, 57–80.

Masoud, A. & Koike, K., 2006. Tectonic architecture through Landsat-7 ETM+/SRTM DEM-derived lineaments and relationship to the hydrogeologic setting in Siwa region, NW Egypt. *Journal of African Earth Sciences* 45, 467–477.

Michard, A., Saddiqi, O., Chalouan, A. & Frizon de Lamotte, D., 2008. *Continental evolution: The geology of Morocco. Structure, stratigraphy, and tectonics of the Africa-Atlantic-Mediterranean Triple Junction*. Lecture Notes in Earth Sciences Book Series. 424 pp.

Missenard, Y., Taki, Z., Frizon de Lamotte, D., Benammi, M., Hafid, M., Leturmy, P. & Sébrier, M., 2007. Tectonic styles in the Marrakesh High Atlas (Morocco): The role of heritage and mechanical stratigraphy. *Journal of African Earth Sciences* 48, 247–266.

Morsli, Y., Zerhouni, Y., Maimouni, S., Alikouss, S., Kadir, H. & Baroudi, Z., 2021. Pegmatite mapping using spectroradiometry and ASTER data (Zenaga, Central Anti-Atlas, Morocco). *Journal of African Earth Sciences* 177, 104153.

Muavhi, N. & Mavhungu, M.E., 2020. Mapping of gold-related alteration minerals and linear structures using ASTER data in the Giyani Greenstone Belt, South Africa. *South African Journal of Geomatics* 9, 250–266.

Othman, A.A. & Gloaguen, R., 2017. Integration of spectral, spatial and morphometric data into lithological mapping: A comparison of different Machine Learning Algorithms in the Kurdistan Region, NE Iraq. *Journal of Asian Earth Sciences* 146, 90–102.

Piqué, A., Le Roy, P. & Amrhar, M., 1998. Transtensive synsedimentary tectonics associated with ocean opening: the Essaouira–Agadir segment of the Moroccan Atlantic margin. *Journal of the Geological Society* 155, 913–928.

Pour, A.B. & Hashim, M., 2015. Integrating PALSAR and ASTER data for mineral deposits exploration in tropical environments: a case study from Central Belt, Peninsular Malaysia. *International Journal of Image and Data Fusion* 6, 170–188.

Rowan, L.C., Kingston, M.J. & Crowley, J.K., 1986. Spectral reflectance of carbonatites and related alkalic igneous rocks; selected samples from four North American localities. *Economic Geology* 81, 857–871.

Salisbury, J.W. & Walter, L.S., 1989. Thermal infrared (2.5–13.5 μm) spectroscopic remote sensing of igneous rock types on particulate planetary surfaces. *Journal of Geophysical Research* 94, 9192.

Schwarz, G. & Wigger, P.J., 1988. Geophysical studies of the Earth's crust and upper mantle in the Atlas system of Morocco. [In:] Jacobshagen, V.H. (Ed.): The Atlas System of Morocco, Lecture Notes in Earth Sciences. Springer-Verlag, Berlin, pp. 339–357.

Sheikhrahimi, A., Pour, A.B., Pradhan, B. & Zoheir, B., 2019. Mapping hydrothermal alteration zones and lineaments associated with orogenic gold mineralization using ASTER data: A case study from the Sanandaj-Sirjan Zone, Iran. *Advances in Space Research* 63, 3315–3332.

Shirmard, H., Farahbakhsh, E., Beiranvand Pour, A., Muslim, A.M., Müller, R.D. & Chandra, R., 2020. Integration of selective dimensionality reduction techniques for mineral exploration using ASTER satellite data. *Remote Sensing* 12, 1261.

Sintubin, M., Nefly, M., Rijpens, J. & Zegbroek, B.V., 1997. Faulting history at the eastern termination of the High Atlas Fault (Western High Atlas, Morocco). *Geologie en Mijnbouw* 76, 187–195.

Skikra, H., Amrouch, K., Soulaimani, A., Leprêtre, R., Ouabid, M. & Bodinier, J.-L., 2021. The intracontinental High Atlas belt: geological overview and pending questions. *Arabian Journal of Geosciences* 14, 1071.

Syzdykbayev, M., Karimi, B. & Karimi, H.A., 2020. A method for extracting some key terrain features from shaded relief of digital terrain models. *Remote Sensing* 12, 2809.

van Andel, T.H., 1998. Book review: Ruddiman, W.F. (Ed.) 1997. Tectonic uplift and climate change. Plenum Press. *Geological Magazine* 135, 819–820.

Zhao, Z.-F., Zhou, J.-X., Lu, Y.-X., Chen, Q., Cao, X.-M., He, X.-H., Fu, X.-H., Zeng, S.-H. & Feng, W., 2021. Mapping alteration minerals in the Pulang porphyry copper ore district, SW China, using ASTER and WorldView-3 data: Implications for exploration targeting. *Ore Geology Reviews* 134, 104171.

Manuscript submitted: 1 October 2022
Revision accepted: 25 February 2023